The Astrophysical Journal, 700:292–301, 2009 July 20 doi:10.1088/0004-637X/700/1/292

STEREOSCOPIC POLAR PLUME RECONSTRUCTIONS FROM *STEREO*/SECCHI IMAGES

L. Feng[1,2], B. Inhester[1], S. K. Solanki[1], K. Wilhelm[1], T. Wiegelmann[1], B. Podlipnik[1], R. A. Howard[3], S. P. Plunkett[3], J. P. Wuelser[4], and W. Q. Gan[2]

[1] Max-Planck-Institut für Sonnensystemforschung, Max-Planck-Str.2, 37191 Katlenburg-Lindau, Germany
[2] Purple Mountain Observatory, Chinese Academy of Sciences, 210008 Nanjing, China
[3] Naval Research Laboratory, Code 7660, 4555 Overlook Ave. SW, Washington DC 20375, USA
[4] Solar and Astrophysics Lab., Lockheed Martin ATC, 3251 Hanover St., Palo Alto, CA 94304, USA

Received 2009 February 19; accepted 2009 May 19; published 2009 July 1

ABSTRACT

We present stereoscopic reconstructions of the location and inclination of polar plumes of two data sets based on the two simultaneously recorded images taken by the EUVI telescopes in the SECCHI instrument package onboard the *Solar TErrestrial RElations Observatory* spacecraft. The 10 plumes investigated show a superradial expansion in the coronal hole in three dimensions (3D) which is consistent with the two-dimensional results. Their deviations from the local meridian planes are rather small with an average of 6.°47. By comparing the reconstructed plumes with a dipole field with its axis along the solar rotation axis, it is found that plumes are inclined more horizontally than the dipole field. The lower the latitude is, the larger is the deviation from the dipole field. The relationship between plumes and bright points has been investigated and they are not always associated. For the first data set, based on the 3D height of plumes and the electron density derived from SUMER/*SOHO* Si VIII line pair, we found that electron densities along the plumes decrease with height above the solar surface. The temperature obtained from the density scale height is 1.6–1.8 times larger than the temperature obtained from Mg IX line ratios. We attribute this discrepancy to a deviation of the electron and the ion temperatures. Finally, we have found that the outflow speeds studied in the O VI line in the plumes corrected by the angle between the line of sight and the plume orientation are quite small with a maximum of 10 km s^{-1}. It is unlikely that plumes are a dominant contributor to the fast solar wind.

Key words: methods: data analysis – solar wind – Sun: corona – Sun: magnetic fields – techniques: image processing

Online-only material: color figures

1. INTRODUCTION

With the launch of NASA's *Solar TErrestrial RElations Observatory* (*STEREO)* mission in 2006 October, a new dimension has been added to solar coronal observations. The two spacecraft orbit the Sun and separate slowly in longitude by about 45° per year. The first year after launch is the best time for the three-dimensional (3D) reconstruction of coronal structures, such as magnetic loops (Wiegelmann & Inhester 2006; Feng et al. 2007a, 2007b; Aschwanden et al. 2008b), polar plumes (Curdt et al. 2008), polar jets (Patsourakos et al. 2008), solar prominences (filaments), etc., which can be achieved by analyzing the image pairs taken by the Extreme Ultraviolet Imager (EUVI) telescopes that are part of the SECCHI suite of imagers. EUVI is very similar to EIT/*SOHO*, but with higher spatial resolution (1.″6 per pixel) and larger field of view (out to 1.7 $R_\odot$). For the objectives of the mission and more details about the EUVI telescopes, see Howard et al. (2008) and Wuelser et al. (2004).

As the solar activity was low in 2007, the appearance of the solar corona over the poles was dominated by extended raylike features, the so-called polar plumes. They are believed to trace out open magnetic field lines and have been intensively analyzed in white light, EUV, and soft X-rays. Coordinated observations using the *SOHO* spacecraft and the ground-based HAO (High Altitude Observatory) Mk-3 coronagraph of the polar plumes from the photosphere to approximately 15 $R_\odot$ were presented by DeForest et al. (1997) and out to 30 $R_\odot$ or 45 $R_\odot$ by DeForest et al. (2001). Gabriel et al. (2003, 2005) have suggested that plumes are a substantial contributor to the fast solar wind, whereas Habbal (1992), Wang (1994), and Wilhelm et al. (2000) have a different point of view. They suggest that the interplume regions are the dominant source of the high-speed solar wind. Another debate about plumes is whether they are rooted in a unipolar magnetic field configuration (e.g., Newkirk & Harvey 1968; DeForest et al. 1997) or are formed by the unipolar magnetic field reconnected with emerging bipolar regions (e.g., Wang & Sheeley 1995).

One handicap of all previous studies was the fact that plumes, even though well visible in two-dimensional (2D) images beyond the limb, could not be reliably traced to the solar surface. We have reconstructed the 3D geometry of the polar plumes by analyzing the simultaneously observed EUVI images for two data sets, 2007 April 7 and June 1. Preliminary results of the 3D plume coordinates obtained on one of the studied days (April 7) are shown in Curdt et al. (2008). In this paper, we describe an improved method of stereoscopic reconstruction in detail since in Curdt et al. (2008) the emphasis was put on the multi-spacecraft observations from *Hinode*, *STEREO*, and *SOHO*. Furthermore, based on the 3D coordinates, we have calculated the inclination of plumes to the line of sight (LOS) of the Earth and to their local radial direction for both data sets. We have compared the 3D orientation of plumes with the local direction of a dipole magnetic field. The dipole field is the lowest order approximation of the coronal magnetic field at times of low solar activity when the plume observations were made. Additionally, we have calculated the footpoint positions of the reconstructed plumes and projected them onto the EUVI images to investigate their relationship to EUV bright points. For the first data set, *SOHO*/SUMER observations were also available. We have used them to determine physical parameters, including the temperature, density, and LOS Doppler shift. By projecting

Table 1
The Positions of the Two *STEREO* Spacecraft Given in the HEEQ Coordinate System, Exposure Time of the Observation, and Compression Mode of the Recorded Data on 2007 April 7 22:01:17 UTC and on 2007 June 1 00:09:00 UTC

Date	2007 April 7		2007 June 1	
STEREO spacecraft	B	A	B	A
Sun–Earth. dist., d (au)	1.0277777	0.9640101	1.0647322	0.95860281
Sun's app. rad., $R_\odot$ ($''$)	933.69200	995.45200	901.28300	1000.3757
HEEQ longitude, φ ($^\circ$)	−0.918945	2.697643	−3.6847666	6.7788499
HEEQ latitude, θ ($^\circ$)	−6.404608	−5.999570	−1.4801556	0.2276848
resolution, Δx ($''$pixel^{-1})	1.5900000	1.5877700	1.5900000	1.5877740
Separation, α ($^\circ$)	3.62		10.6	
Exposure time, T (s)	20		16	
Compression mode	ICER4		ICER4	

a 3D plume onto the SUMER density map, its density scale height could be calculated. The temperature corresponding to this scale height and the temperature derived spectroscopically from SUMER have been compared.

2. THE DATA

STEREO was launched somewhat after the solar activity minimum which provides us with good opportunities to observe polar plumes. We selected two data sets for this study, one in the south polar cap on 2007 April 7 22:01:17 UTC and the other in the north polar cap on 2007- June 1 00:09:00 UTC. Both were recorded by the two almost identical SECCHI/EUVI telescopes at $\lambda = 17.1$ nm corresponding to a formation temperature of roughly 1 MK. The position information of both spacecraft, the exposure time, and the compression mode are given in Table 1.

On April 7, the separation of the two spacecraft was 3.°6. The HEEQ (Heliocentric Earth EQuatorial coordinate system; Thompson 2006) latitudes of the two spacecraft were well below the Sun's equatorial plane. At that time the solar south pole was tilted toward the spacecraft which was very appropriate for observing as much as possible of the southern polar area. In addition, to improve the signal-to-noise ratio of the EUVI images, a longer exposure time and a smaller compression were applied. The image pairs chosen in this work have 20 s exposure time, compared to the normal exposure time of 2 s. The images were compressed by the format ICER (a wavelet-based image compression file format) 4 which requires two times the storage of images obtained after applying the usual ICER 6 compression used ordinarily for EUVI images at 17.1 nm. In Figure 1, the southern polar cap in both EUVI views is presented with five plume pairs marked by numbers below them.

In parallel, SUMER performed a raster scan from 2007 April 7 01:01 UTC to 2007 April 8 12:19 UTC in the southern corona. The scan direction was from solar west to east. The details of the SUMER observations can be found in Curdt et al. (2008). To combine with 3D plume geometry, we derived the electron density map from the emission line pair Si VIII at 144.0 nm and 144.6 nm, the electron temperature map from line pair Mg IX at 70.6 nm and 75.0 nm, and the LOS Doppler shift map from the O VI at 103.2 nm and 103.8 nm.

The second analyzed EUVI data set was recorded on June 1 (Figure 2), when the separation angle between the spacecraft was 10.°6. This increased separation angle reduced the reconstruction uncertainty considerably. At the same time, this separation angle is still sufficiently small so that the correspondence between individual plumes in both EUVI images can still be unambiguously identified. The related spacecraft positions, observation, and compression parameters are listed in Table 1.

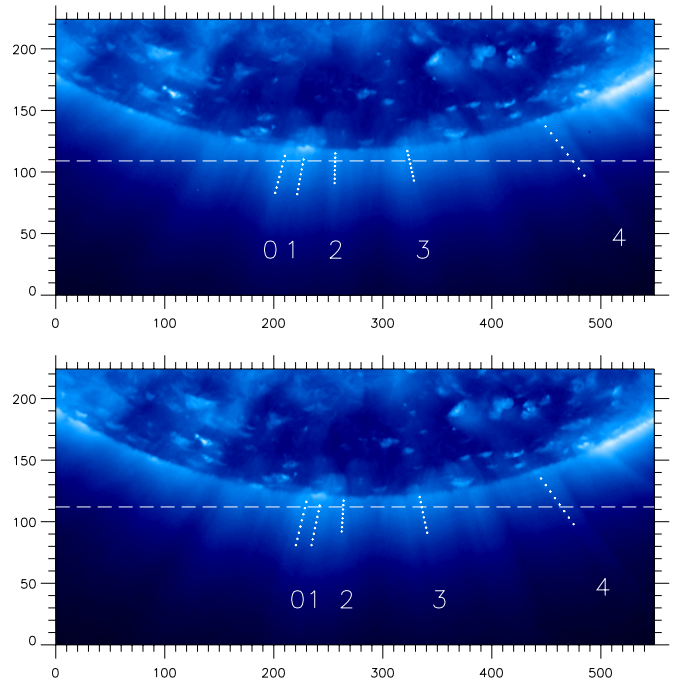

Figure 1. South polar cap observed on 2007 April 7 22:01:17 UTC at $\lambda = 17.1$ nm by EUVI A (upper) and B (bottom). The corresponding epipolar lines are approximated by the two long-dashed lines. The dotted lines are the identified plumes (see Section 3 for details).

(A color version of this figure is available in the online journal.)

3. THE RECONSTRUCTION

To reconstruct the 3D geometry of the plume, the first step is to identify the points along the plume axis and associate the corresponding plume pair in the two simultaneous EUVI images. To establish this correlation between the plumes, we extracted from each image the radiance profiles along corresponding epipolar lines (Inhester 2006) in both images. Figure 3 gives an example for the April 7 data. The radiance distributions along the corresponding epipolar lines, which are approximated by the two long-dashed lines in Figure 1, were smoothed by taking the running mean of the radiance over three pixels. The plume centers were selected according to the local radiance maxima and marked by the corresponding numbers.

For plumes 0, 1, 2, and 4 the association is clear. However, for plume 3 there is some uncertainty due to the complicated superposition of probably several plumes along the LOS. The radiance distribution around plume 3 in EUVI A is dominated by one prominent peak (marked as 3a in Figure 3) with a

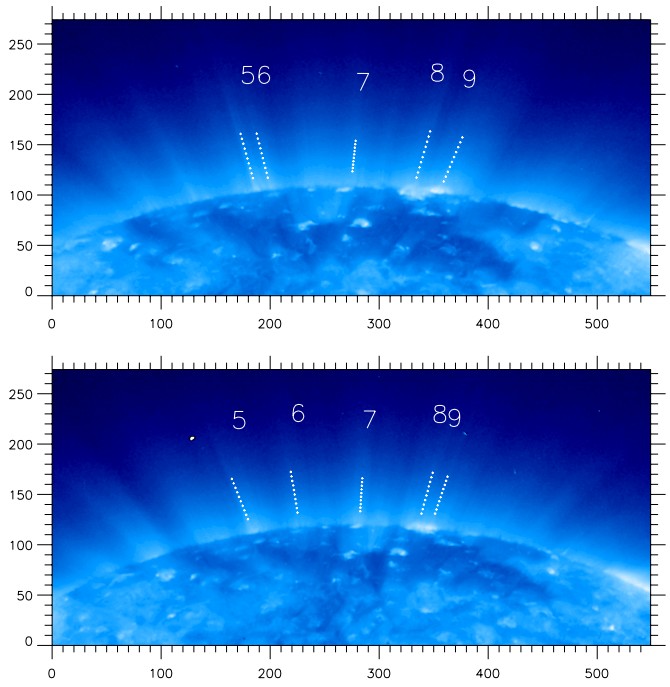

Figure 2. North polar cap observed at 2007 June 1 00:09:00 UTC by EUVI A (upper) and B (bottom).

(A color version of this figure is available in the online journal.)

smaller peak (3) on the right side, whereas in EUVI B two distinct peaks (3b and 3) appear. There are four possible ways to associate the two plume signatures in the two images. Trying all combinations, we judged their likelihood from the inclination of the resulting 3D plumes. When a point on the 3D plume leaves from its footpoint on the solar surface, its distance to the solar rotation axis should increase as well. The second criterion is that the angle between the plume and the local meridian plane passing through the plume footpoint should be as small as possible (see Figure 7). In this way, we find that the combination of peak 3 in image A and peak 3 in image B gave the most reasonable result. In Figure 4, we sketch the situation which we think yields the different peaks in the two images for plume 3. Here we assumed a circular shape and a uniform radiance distribution within the cross section of two plumes of different radii. Figure 4 shows the resulting radiance distributions from two different perspectives.

Finally, the axes of the five plumes were traced by repeating the procedure for each plume at eight different heights above the solar limb. Since in EUV images plumes are shaped as nearly straight lines, each plume axis was approximated by a linear function and is plotted as a dotted line in Figure 1. The identification of the plumes for the second data set observed in 2007 June is similar and the results are overplotted on the corresponding EUVI A and B images shown in Figure 2.

From these linear 2D plume positions in both EUVI images, we reconstruct the 3D plume locations based on epipolar geometry in the frame of the HEEQ coordinate system. The reconstructed plumes are straight lines in 3D. In order to obtain an error estimate, we here assume a maximal uncertainty of 3 Mm, corresponding to an positional error in the images of 4.″3 in EUVI A and 4.″0 in EUVI B, in the estimated plume position along the epipolar line due to the three-pixel smoothing as mentioned before. We shall see in the next section that this uncertainty is propagated to an analogous uncertainty of the stereoscopic reconstruction.

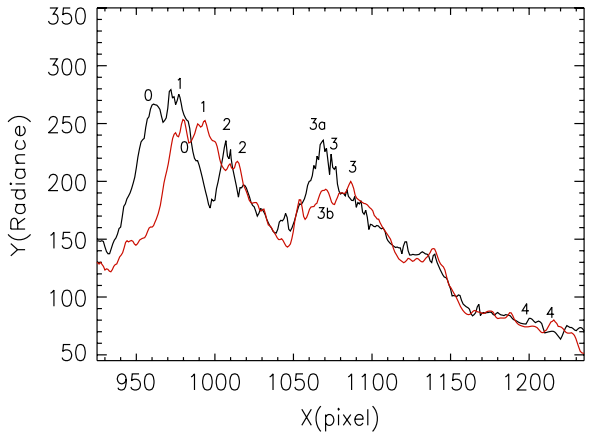

Figure 3. Radiance distributions smoothed over three pixels along the corresponding epipolar lines in each EUVI image observed in April. The black and red lines are for EUVI A and B, respectively. The x coordinate of the solar center in A and B lies at 1020.62 and 1035.52 in units of pixels, respectively. The numbers refer to the plumes in Figure 1.

(A color version of this figure is available in the online journal.)

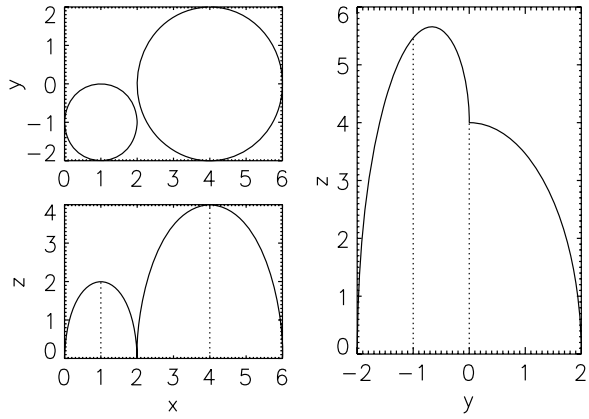

Figure 4. Schematic explanation of why a different number of peaks might be visible from different perspectives. The upper left panel shows the assumed cross section of two plumes. The lower left panel displays the LOS integrated radiance as seen in the y-direction, The right panel exhibits the radiance as seen along the x-direction.

4. RESULTS

We present the different perspectives of plumes for two data sets derived from stereoscopic reconstructions in Section 4.1, as well as the plume orientation analyses, plume width calculations, and the relationship between plumes and EUV bright points. In Section 4.2 the results obtained by combining stereoscopic reconstructions and the plume density and temperature deduced from SUMER observations are shown. The density scale height and its corresponding temperature are calculated by assuming that the plume in our study is in hydrostatic equilibrium.

4.1. Stereoscopic Results

4.1.1. Side View and Top View

In Figure 5, we present a view of the 3D placement and direction of polar plumes from a perspective that is 90° to the left and 20° up compared to the view direction of *STEREO A*. Of the five reconstructed plumes in April, three are in front of the solar limb as seen from *STEREO A*, the other two are behind the limb. For the data set in June, only plume 6 lies in front of solar

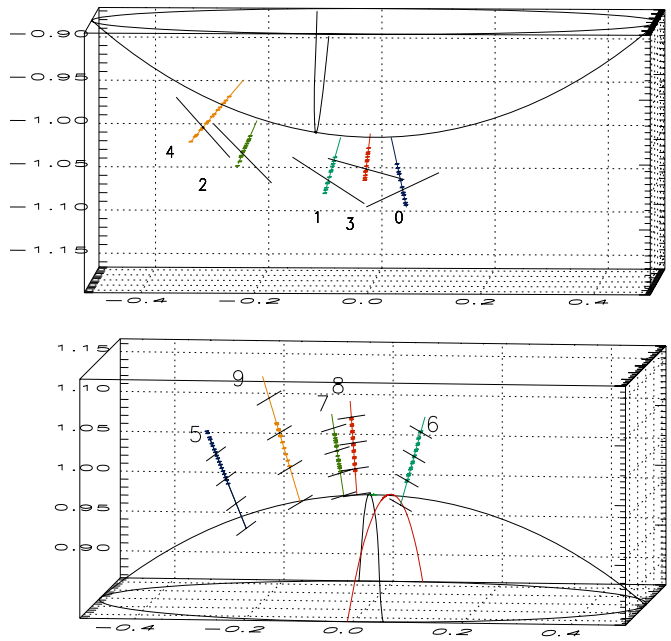

Figure 5. Side view of the south polar cap on April 7 (upper panel) and the north polar cap on June 1 (lower panel): a perspective that is 90° to the left, and 20° up relative to the view direction of *STEREO* A. The coordinates x and y range from -0.5 $R_\odot$ to 0.5 $R_\odot$, z ranges from -0.87 $R_\odot$ to -1.17 $R_\odot$ for the south polar cap and from 0.87 $R_\odot$ to 1.17 $R_\odot$ for the north cap. The long curve is a circular segment crossing the pole. The shorter curves are the solar limbs as seen from the two spacecraft (black from *STEREO A* and red from *STEREO B*). The dotted points are the reconstructed 3D plume axes. The solid lines are the extrapolations back to $r = 1$ $R_\odot$. The uncertainties are indicated by the black solid lines which are perpendicular to the plume directions in 3D.

(A color version of this figure is available in the online journal.)

limbs as seen by both spacecraft. The black solid lines indicate the reconstruction uncertainties (Inhester 2006) calculated by assuming a maximal 3 Mm variation of the plume axis position. The resulting uncertainties are directed mainly half way between the view directions of *STEREO A* and *B*, and are considerable for the data set in April since the spacecraft separation angle was small at that time. With the increased separation angle in June, the uncertainties are greatly reduced for the same assumption of 3 Mm uncertainty in 2D.

The polar view of the 10 plumes projected onto the solar equatorial plane is shown in Figure 6. Larger symbols indicates the plume positions at greater heights above the solar surface. All 10 plumes oriented close to their local meridian planes and inclined away from the rotation axis.

4.1.2. Plume's Orientation Analysis

In Figure 7 a sketch of the 3D plume geometry is presented to analyze the plume orientation. The relevant results are shown in Table 2. Concerning the latitudes and longitudes of the plume footpoints, all the plumes are located within a latitude cone of 20° around the pole. For a better estimate of the outflow speeds along the plumes from far ultraviolet (FUV)/EUV spectral observations by SUMER and UVCS on board *SOHO*, the angle β between the LOS from the Earth and the plumes' orientation were calculated. They range from 65.°7 to 128.°6 for plumes 3 and 8, being almost perpendicular to the view direction of the Earth. For the angle γ off the meridian plane, we found for all 10 plumes a maximum departure of 14.°2. This indicates that the magnetic azimuthal component B_φ was very small on the polar cap during the time of our observations. The deviation of the plume projection to the solar radial direction $\widehat{\mathbf{e}}_\mathbf{r}$ is calculated and represented by the angle ψ. This angle in general becomes larger with increasing distance of the footpoint from the pole, as shown in the upper panel of Figure 8. This means that the plumes do not converge to the solar center, which is consistent with the 2D results (DeForest et al. 1997; Fisher & Guhathakurta 1995). They found that the plumes/rays appear to diverge radially from a point between the solar center and the respective pole.

In addition, we compared the 3D plume structure which outlines the coronal magnetic field with the assumption of a dipole with its axis along the solar rotation axis. In this case the plume's inclination angle i and the footpoint latitude λ should be related by $\tan i = 2 \tan \lambda$ (see page 50 of Fowler 1990). From the related two rows in Table 2 we find that this relation is not well satisfied for each plume and $|\tan i| < 2|\tan \lambda|$ in all cases.

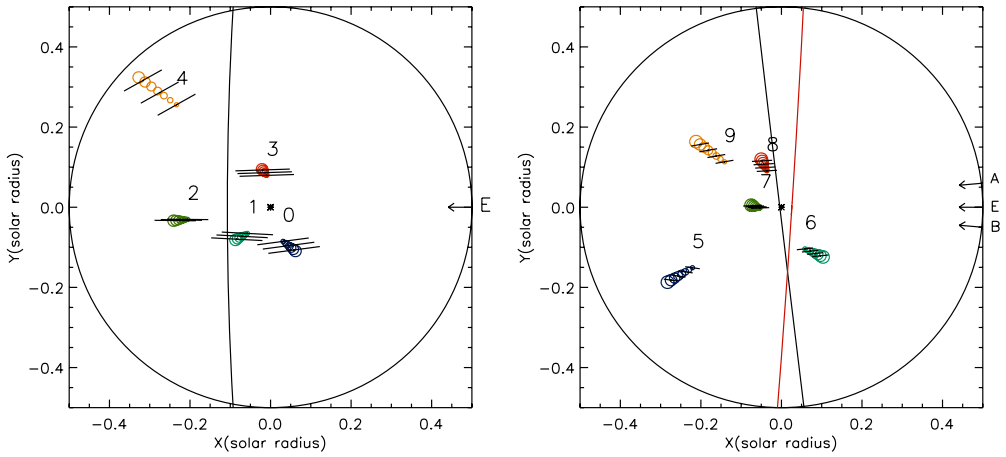

Figure 6. Top view: projections of the reconstructed 3D plumes onto the solar equatorial plane in April (left) and June (right) together with the associated uncertainties (black solid lines). For each plume, the size of the circle is proportional to the distance of the 3D point to the solar surface. In the left panel, the solar limb as seen from the Earth is indicated by the curve near the pole which is marked by a star symbol. The view direction from the Earth indicated by the arrow marked E at the right edge of the figure is also shown. In the right panel, the solar limb as seen from *STEREO A* is indicated by a black curve and seen from *STEREO B* is indicated in red. The view directions of the two spacecraft and the Earth are marked on the right side.

(A color version of this figure is available in the online journal.)

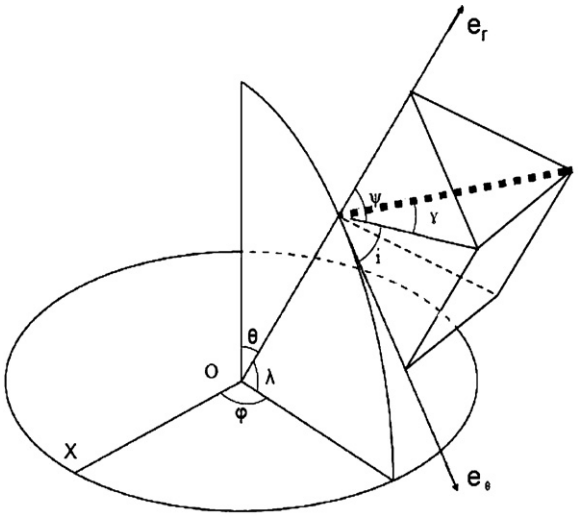

Figure 7. Schematic illustration of 3D plume geometry in the HEEQ coordinate system. The 3D plume is indicated by the thick dashed line started from the solar surface. The plume footpoint is parameterized with the longitude φ and latitude λ (the colatitude is denoted as θ). We establish the local coordinate framed by $\widehat{\mathbf{e}_r}$, $\widehat{\mathbf{e}_\theta}$ and $\widehat{\mathbf{e}_\varphi}$ (for clearness of this figure $\widehat{\mathbf{e}_\varphi}$ is not shown) which originates from the footpoint. The projection of the 3D plume onto the local meridian plane spanned by $\widehat{\mathbf{e}_r}$ and $\widehat{\mathbf{e}_\theta}$ makes two angles: ψ is the angle between the projection and $\widehat{\mathbf{e}_r}$, i is the angle between the projection and $\widehat{\mathbf{e}_\theta}$ and is the so-called magnetic inclination. γ is the angle between the 3D plume and its projection mentioned above.

Therefore the magnetic field is not well approximated by this dipole field and is more horizontal, as also shown in the middle panel of Figure 8. In the bottom panel we check how much plumes deviate from the dipole field and how this deviation changes with the latitude. We find that at lower latitudes the plumes are more horizontal than the dipole field. This was already noted by Saito (1965) who used a bar magnet of finite length to fit the plumes/rays at different distances from the Sun observed during a solar eclipse. Banaszkiewicz et al. (1998) described a simple analytic model for the magnetic field at solar activity minimum. A dipole and a quadruple field were added to construct the coronal magnetic field in the solar minimum. The reconstructed 3D plumes could be used as a reference in the polar region to test other, more sophisticated magnetic field models (Neukirch 1995; Ruan et al. 2008).

4.1.3. Plume's Width Analysis

Besides the orientation, we calculated the width of the isolated and prominent plume 4 from viewpoints of EUVI A and B by fitting the radiance profiles around this plume with Gaussian distributions. For the plume width w at a given height h we use the definition of Aschwanden et al. (2008a):

$$w(h) = \frac{\int_{x_{b1}}^{x_{b2}} [I(h,x) - b(h,x)]\mathrm{d}x}{\max[I(h,x) - b(h,x)]}, \quad (1)$$

where x_{b1} and x_{b2} are the x coordinates of the two plume boundary points determined by the two local minima on either side of the plume (Figure 9). Here, $b(h,x)$ is the linearly varying background radiance between x_{b1} and x_{b2}. $I(h,x) - b(h,x)$ then denotes the background subtracted plume radiance distribution as a function of height h. The intensities associated with this plume along two epipolar lines are shown in Figure 9 as an example. By using the epipolar geometry, we identify the corresponding plume point in two images and calculate the plume width from EUVI A and EUVI B, respectively. Subsequently the plume widths along the corresponding epipolar lines are transformed to the widths perpendicular to the plume direction within the frame of the epipolar geometry.

For this plume, we found from both viewpoints that the width very slightly decreases by around 10% in the height range from 20 Mm to 90 Mm in 3D. The mean width and standard deviation from EUVI B is (14.0 ± 0.9) Mm, while from A it is (12.7 ± 1.2) Mm. The two widths differ by less than 1.5 σ so that this measurement is consistent with a circular plume cross section. However, given the small separation angle, a more curtain-like structure cannot be ruled out either. More isolated and prominent plumes need to be analyzed at large separation angles to come to a conclusion regarding the cross section of the plumes. It should be mentioned here that we have only considered the circular or simple noncircular cross sections for plumes and we have not taken into account the substructure that is known to exist within plumes (e.g., DeForest 2007; DeForest et al. 1997). Unresolved morphology can mimic a surprising range of other effects including modifying the inferred density (both from photometric density estimates and from line-ratio estimates, in different ways for the two techniques) and the observed scale height.

Table 2
Footpoint Position and Inclination of the Reconstructed Plumes on April 7 and on June 1

Date	April 7					June 1				
Plume	0	1	2	3	4	5	6	7	8	9
λ (°)	−84.7	−85.0	−78.0	−85.4	−69.7	74.5	83.2	86.9	84.4	79.6
φ (°)	−69.9	−131.3	−171.6	96.9	132.5	−145.6	−60.7	−177.9	111.7	141.3
β (°)	65.7	106.7	117.4	94.4	128.6	118.8	68.6	103.2	97.6	114.8
γ (°)	12.2	−8.61	−1.70	8.67	9.85	−2.25	14.2	−4.48	1.10	1.62
ψ (°)	−15.0	−19.9	−21.9	−10.4	−37.0	17.4	13.2	9.35	10.4	19.6
$\tan(i)$	−3.73	−2.77	−2.52	−5.45	−1.32	3.19	4.26	6.07	5.43	2.80
$2\tan(\lambda)$	−21.9	−22.3	−9.40	−24.9	−5.42	7.20	16.7	37.5	20.4	10.9
$(i - i')$ (°)	12.4	17.3	15.8	8.10	26.5	−9.49	−9.77	−7.82	−7.59	−14.4

Notes. The relevant angle symbols are the same as defined in Figure 7. The first two rows are the footpoint latitudes and longitudes of the plumes. β gives the angle between a plume orientation and the LOS direction of the Earth. γ measures how much a plume deviates from the local meridian plane and its sign depends on the sign of $\widehat{\mathbf{e}}^T_{\mathrm{plume}} \cdot \widehat{\mathbf{e}_\varphi}$. ψ is the complementary angle of magnetic inclination i and its sign is the same as the sign of $\widehat{\mathbf{e}}^T_{\mathrm{plume}} \cdot \widehat{\mathbf{e}_\theta}$. All angles are given in units of degrees. The last three rows are the tangent of magnetic inclination, two times the tangent of the latitude, the difference of the magnetic inclination i with the dipole magnetic inclination i' corresponding to $\arctan(2\tan\lambda)$.

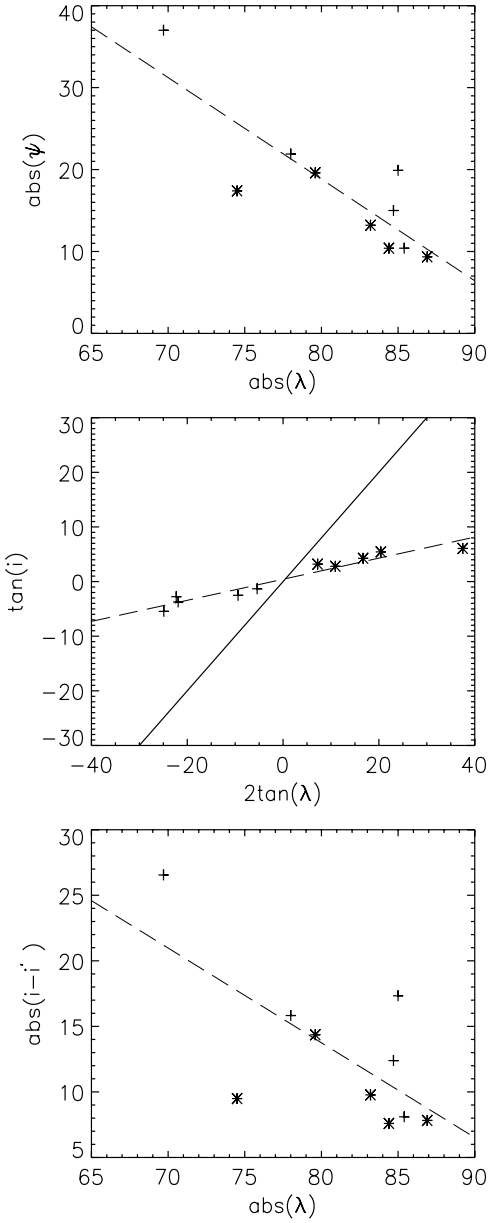

Figure 8. Upper: absolute value of ψ as a function of the absolute value of λ. The plus signs are for the data in April and star signs for the data in June. Middle: the plot of $\tan(i)$ vs.$2\tan(\lambda)$. The solid line corresponds to $\tan(i) = 2\tan(\lambda)$. Bottom: the difference of the magnetic inclination i from the dipole field inclination i' as a function of the absolute latitude.

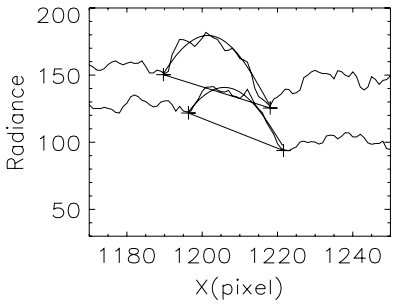

Figure 9. Radiance profile around plume 4 along two epipolar lines in EUVI B. On each line the two plus signs indicated the plume boundary and the connected straight line shows the plume background. Within the range between the two boundary points, the radiance is fitted by the Gaussian distribution.

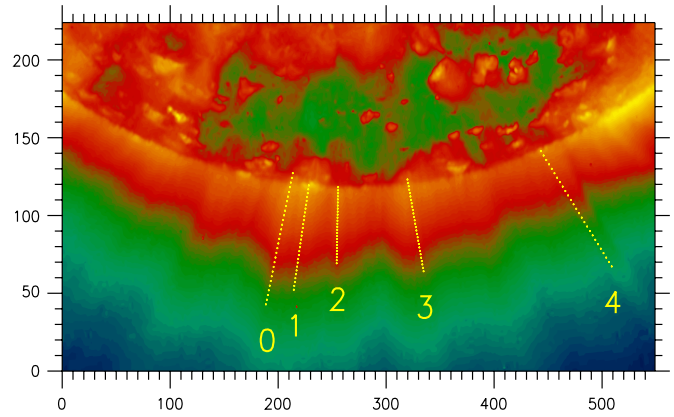

Figure 10. Projection of the 3D plumes onto the image of EUVI A observed on April 7.

(A color version of this figure is available in the online journal.)

4.1.4. Plume and EUV Bright Points

To investigate the relationship between plumes and EUV bright points, we projected the reconstructed 3D plumes onto two EUVI images. For the data in April, given the small separation angle, only the projection onto EUVI A is plotted in Figure 10. Only plume 1 is associated with a bright point. Plumes 0 and 3 were rooted in the brighter part of the coronal hole, but not on a bright point. Considering the evolution of polar plumes (Wang 1998; Raouafi et al. 2008), plumes 0 and 3 were observed perhaps in the decaying phase in which the bright points have already disappeared but the two plumes were still visible. For the big bright point close to the limb between plumes 3 and 4, we tried to find a plume pair but none of the possible peaks in the two plume radiance profiles (e.g., Figure 3) produced a reasonable result with a footpoint close to this bright point and an orientation roughly along the diverging direction of the magnetic field around the pole.

For the data in June, Figures 5 and 6 reveal that of the five reconstructed plumes only plume 6 lies in front of the solar limbs as seen by *STEREO A* and *B*, the footpoints of the other four are hidden by the limb. By projecting the reconstructed plumes onto two simultaneous EUVI images (see Figure 11) and taking into account Figures 5 and 6, the spatial relationship between plumes and bright points can be inferred. The plume in front of both limbs, that is, plume 6 could be associated with a very faint bright point. Plume 7 presents a nice example of the importance of having 3D information when associating plumes with bright points. If we consider only EUVI B, then plume 7 seems to be related to a bright point right in front of the limb. However, when we check both Figures 5 and 6 we find this plume is rooted just behind the limbs seen by EUVI A and B. Therefore, the association to the bright point near the limb is probably spurious. For plumes 8 and 9, it is difficult to reach a firm conclusion. We see two bright points in both images close to the plume roots. The association is possible if the bright point relevant to plume 8 is big enough and the height of the bright point relevant to plume 9 is large enough that it could be seen from EUVI A and B, even though it is behind the limb.

4.2. Results Combining Stereoscopy and SUMER Observations

For the data set in April, SUMER observations are available. To obtain the electron density and electron temperature along a plume, we assume that the geometry of a plume does not change during its evolution, and then project it onto the density

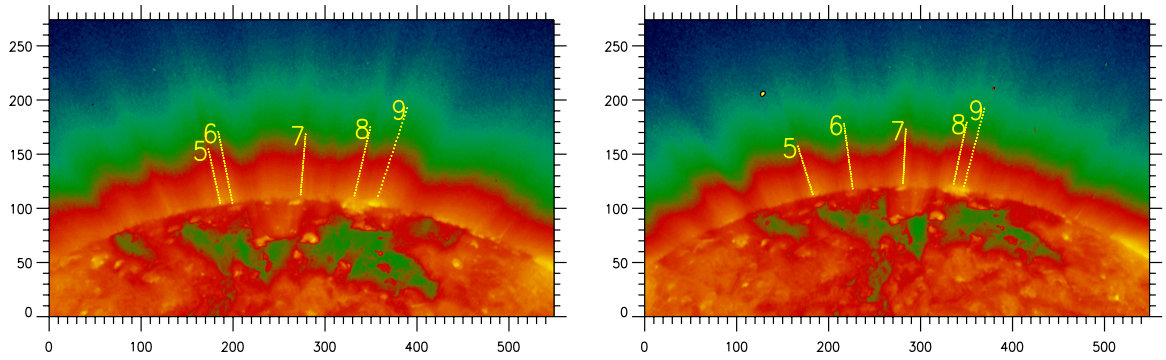

Figure 11. Projections of the 3D plumes on EUVI A and B recorded on June 1.

(A color version of this figure is available in the online journal.)

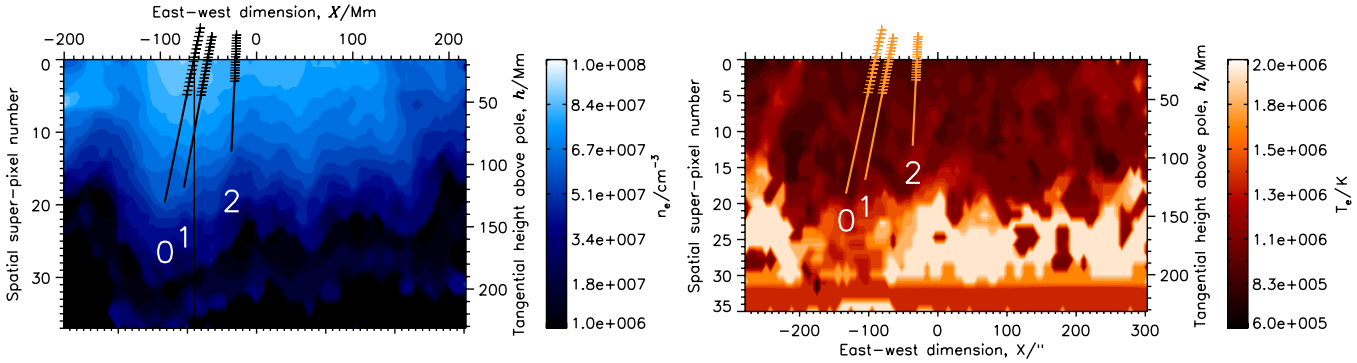

Figure 12. Projections of the 3D plumes 0, 1, and 2 onto the SUMER electron density (upper) and temperature (lower) map with the marked plume numbers. The vertical solid line in the density map corresponds to the position of SUMER slit at April 8 01:00 UTC. The plus signs are the projections of the 3D plumes reconstructed from two EUVI images recorded on April 7 and solid lines are the extrapolations downward to the point where the standard deviation of the temperature along the plume is around 0.1 MK.

(A color version of this figure is available in the online journal.)

and temperature maps deduced from the line ratio of the Si VIII line pair and the Mg IX line pair, respectively (Wilhelm 2006; Wilhelm et al. 2009). Consistent with the previous results, the plumes are denser and cooler than the interplume regions. We deduced the Doppler shift measurements from the O VI lines based on the method outlined in Wilhelm et al. (1998).

SUMER scanned the relevant region from April 7 01:01 UTC to April 8 12:19 UTC continuously moving from west to east. To compare these data with the EUVI observations of a 3D plume, we need to first rotate the Sun from the EUVI observations to the time at which SUMER scanned it. An example is shown in the density map in the upper panel of Figure 12. The inclined lines are the projected positions of three plumes. The vertical line corresponds to the position of the SUMER slit at April 8 01:00 UTC. Consider plume 1, the plotted location was obtained by first rotating the Sun to this time and then projecting plume 1 onto the density map. From Figure 12 we can see that the projected plume 1 and the corresponding slit position are consistent.

The times at which the SUMER slit scanned through the centers of the three plumes 0, 1, and 2 are April 8 02:00 UTC, April 8 01:00 UTC, and April 7 22:00 UTC. They were less than 4 hr after the EUVI observations. Due to the inclination of these three plumes, they are scanned by SUMER for about 2.5 hr, 2 hr, and 1 hr, respectively. We have checked the EUVI images at April 8 02:00 UTC, April 8 01:00 UTC and found that plumes 0 and 1 were still present though the plumes appeared more diffuse at 02:00 UTC. For plume 3, we could not make a comparison because the time difference between the EUVI observation and the corresponding time at which it was scanned by SUMER is too large. Plume 4 in the EUVI observation lies outside the field of view of the SUMER scan. In Figure 12, the plus signs are the projections of the 3D plumes reconstructed from two EUVI images, the solid lines are their extrapolations outward. We somewhat arbitrarily choose the upper end of height profile where the temperature by SUMER does not dramatically deviate from 0.9 MK or so. It makes the plumes more or less isothermal, which is an assumption for the later calculations. Furthermore, above ≈120 Mm the temperature plot is too noisy for a quantitative analysis. For the density, ≈150–170 Mm might be an approximate limit.

We projected a 3D plume onto LOS Doppler shift map as well to get a more precise outflow velocity along the plume by dividing the SUMER velocity with the cosine of the plume inclination angle to the LOS. However, we did not find any significant Doppler shift from SUMER observations; the maximum of the Doppler velocities is around 3 km s^{-1}. If we take this number as a reference to estimate the outflow velocities along the plumes 0, 1, and 2, we found that they are quite small with a maximum of 10 km s^{-1}. This speed is much smaller than the sound speed $c_s \approx 140$ km s^{-1} for a temperature of ≈0.9 MK.

Similar to Gabriel et al. (2003), we have made an estimate of the plume contribution to the fast solar wind. The proton flux density for the high-latitude fast solar wind observed during the solar minimum from Ulysses at $r_E = 1$ AU is

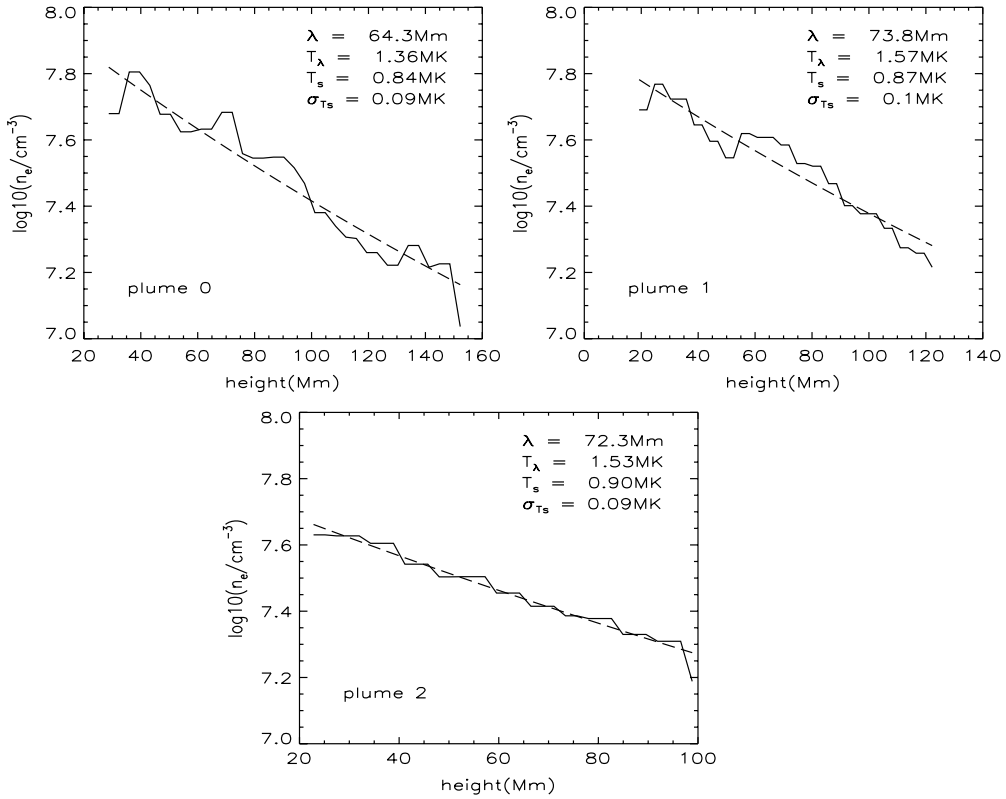

Figure 13. Logarithmic electron density along the plumes 0, 1, 2 from SUMER observation as a function of height above the solar surface as deduced from stereoscopic reconstructions (solid lines). The dashed lines are fits based on hydrostatic equilibrium described by Equation (7). In the upper right of each figure we mark the numerical values for λ (density scale height), T_λ (temperature corresponding to scale height), T_s (electron temperature from SUMER), and its standard deviation σ_{Ts}.

2.05×10^8 cm^{-2} s^{-1} (McComas et al. 2000). We take the cross sectional area of the coronal hole from Munro & Jackson (1977) that matches the observed values extremely well,

$$A(r) = A_0 \left(\frac{r}{r_0}\right)^2 f(r), \tag{2}$$

where the subscript 0 refers to quantities evaluated near the solar surface and $f(r)$ is the area expansion factor which reaches an almost constant value of 7.26 beyond 3 $R_\odot$. Therefore, the mean proton flux density mapped to the solar surface in the coronal hole is

$$\frac{2.05 \times 10^8 \times A(\mathrm{r_E})}{A_0} = 2.05 \times 10^8 \times \left(\frac{\mathrm{r_E}}{r_0}\right)^2 \times 7.26 \text{ cm}^{-2} \text{ s}^{-1} \approx 6.88 \times 10^{13} \text{ cm}^{-2} \text{ s}^{-1}. \tag{3}$$

On the other hand, the electron flux density contributed by plumes are estimated by taking the maximal density in Figure 13 and maximal velocity of 10 km s^{-1}, that is, $10^{7.8}$ cm^{-3} × 10^6 cm s^{-1} ≈ 6.31×10^{13} cm^{-2} s^{-1}. Comparing the mean flux density and the flux density from plumes, we find that the former is a little bit higher than the latter, and taking into account the filling factor of plumes in coronal holes of 10 % (Ahmad & Withbroe 1977), it is unlikely that the plumes investigated in this work are a dominant contributor to the fast solar wind.

We assume that the plume plasma is in hydrostatic balance considering their long lifetime of one or more days and the absence of any measurable flow. However, if the plasma ions are heated by, e.g., ion cyclotron waves a thermodynamic equilibrium does not necessarily exist since the plasma is mainly cooled by a divergent electron heat flux and by inelastic electron collisions with the ions (Tu & Marsch 1997). Following their two-fluid approach, the sum $p = p_i + p_e$ of ion and electron pressure has to obey

$$\frac{d}{dr}(p_i + p_e)(r) = -m_i n g_\odot \frac{R_\odot^2}{r^2}. \tag{4}$$

Quasineutrality in this balance is insured by an ambipolar electric field which cancels when the momentum equations for ions and electrons are added. Here, m_i is the mean ion mass, n the plasma density and $g_\odot$, the gravity acceleration at the solar surface. For the total pressure we have

$$p = p_i + p_e = nk_B(T_i + T_e) = 2nk_B T_\lambda. \tag{5}$$

Insertion and integration yields, changing the variable r to $h = r - R_\odot$,

$$p = p_0 \exp\left(-\frac{m_i g_\odot}{k_B} \int_0^h \frac{R_\odot^2}{T_\lambda (R_\odot + h')^2}\, dh'\right). \tag{6}$$

For the small height range of our observations, we can neglect a possible height variation of T_λ inside the plumes. Then

$$n \simeq n_0 \exp\left(-\frac{m_i g_\odot}{k_B T_\lambda} \frac{h}{(1 + h/R_\odot)}\right) = n_0 \exp\left(-\frac{h}{\lambda_n(T_\lambda)(1 + h/R_\odot)}\right) \tag{7}$$

where the scale height $\lambda_n(T_\lambda)$ depends on $T_\lambda = (T_i + T_e)/2$ and n_0 is the density at $h = 0$ taken to be the base of the

corona. For typical coronal mean mass m_i we have $\lambda_n(T_\lambda) \simeq 47\ \mathrm{Mm}\,(T_\lambda/\mathrm{MK})$ (Aschwanden 2004).

Since we know the density along the plumes from SUMER observations and we know the 3D height from the stereoscopic reconstructions, we can fit these two variables, n_e and h, to derive T_λ and n_0 in Equation (7). In Figure 13, we present the results of fits based on Equation (7) to the density stratification of plumes 0, 1, 2. The calculated density scale height is given along with the corresponding temperature T_λ and the electron temperature deduced from SUMER T_s in Figure 13. We have invariably $T_\lambda > T_s$. The fits describe the data reasonably well suggesting that they are consistent with hydrostatic equilibrium.

5. DISCUSSION AND OUTLOOK

We have reconstructed the three dimensional geometry of 10 polar plumes using simultaneous observations by the two *STEREO* spacecraft. For two different days, the locations of the footpoints of 10 plumes and their inclinations were determined. Even though the statistical basis is small, we find that the plumes we could detect from the EUV images are homogeneously distributed over the polar cap. For both cases, the deviation of the plumes to the local meridian plane is rather small with an average of 6.°47. The deviation of the plume projection onto the local meridian plane from the local radial direction becomes larger in general with increasing distance of the plume from solar poles. For these two data sets, a simple dipole model with its axis along the solar rotation axis for the global magnetic field does, however, not provide a good description of the obtained inclinations. The magnetic field in these two coronal holes were more horizontal than this dipole field by 12.°9 on average. The lower the latitude is, the larger is the deviation from the dipole field.

Moreover, we find that EUV plumes and EUV surface bright points are not always related, which is consistent with the observations of Wang (1998) and Raouafi et al. (2008). Of the three plumes in front of the solar limb on April 7, only one was definitely associated with a bright point. For the other two we did not find a related bright point. Conversely, we saw a bright point in the images to which no plume pair could be assigned to in the two EUVI images. A possible explanation could be that the lifetime of a bright point is shorter than the formation and decay time of a plume. Wang (1998) assumes a bright-point lifetime of around 12 hr, while for plumes he assumes lifetimes around one day. From the case study of June, we find that care is required when paring plumes with bright points. Spatial coincidence in a single image could easily be misleading.

For the data set in April, based on the results of 3D reconstruction and electron temperature, electron density and Doppler shift derived from the SUMER observations, we calculated the density scale height by assuming that a plume is in hydrostatic equilibrium. Using the reconstructed 3D direction of the plumes in space we could set an upper limit of 10 km s^{-1} for the outflow speed along the plumes. The absence of a significant flow in plumes at heights less than 1.2 $R_\odot$ is in agreement with the conclusions of Wilhelm et al. (2000) and Raouafi et al. (2007). The temperatures derived from the density scale height were all in excess of 1 MK, while SUMER derived electron temperatures were well below 1 MK from line ratios of Mg IX. The ratio of the temperature obtained from the scale height, T_λ, to the electron temperature from SUMER, T_s, is $T_\lambda/T_s \approx 1.62$–$1.81$. Recently, Del Zanna et al. (2008) found that the coronal electron temperatures derived from the Mg IX line ratio may have been significantly underestimated. A coronal hole interplume temperature of 0.85 MK is now revised to 1.16 MK. This conclusion would reduce the discrepancy between the temperatures derived from the two techniques in our work, but would not eliminate it entirely. Even with this correction, $T_\lambda/T_s \approx 1.32$ to 1.46 remains. A possible explanation for this difference of T_λ and T_s could be a deviation of electron and ion temperatures. The scale height depends on the average of the electron and the ion temperature while the Mg IX line-ratio depends on the electron temperature. The corrected ratio of T_λ to T_s corresponds to a ratio of the ion temperature to the electron temperature of from 1.64 to 1.92, which is qualitatively consistent with the result of Wilhelm (2006) derived from a different method. The effective ion temperatures he deduced from the line widths are higher than the electron temperatures as well.

This study has demonstrated that it is possible to uniquely obtain the location and inclination of plumes from stereoscopic reconstructions. These properties can significantly enrich our knowledge of plumes, in particular when combined with other type of data, such as FUV spectra (as shown here) or magnetograms (not shown here). Further stereoscopic reconstructions of a large number of plumes would be very valuable.

The authors appreciated the constructive comments of the referee. *STEREO* is a project of NASA, *SOHO* a joint ESA/NASA project. L.F. and K.W. are members of an ISSI International Study Team on plumes. L.F. was supported by the IMPRS graduate school run jointly by the Max Planck Society and the Universities Göttingen and Braunschweig. T.W. was supported by DLR grant 50OC0501 and W.Q.G. was supported by the National Basic Research Program of China (2006CB806302).

REFERENCES

Ahmad, I. A., & Withbroe, G. L. 1977, Sol. Phys., 53, 397
Aschwanden, M. J. Physics of the Solar Corona: An Introduction (Chichester: Praxis Publishing Ltd)
Aschwanden, M. J., Nitta, N. V., Wuelser, J.-P., & Lemen, J. R. 2008a, ApJ, 680, 1477
Aschwanden, M. J., et al. 2008b, ApJ, 679, 827
Banaszkiewicz, M., Axford, W. I., & McKenzie, J. F. 1998, A&A, 337, 940
Curdt, W., Wilhelm, K., Feng, L., & Kamio, S. 2008, A&A, 481, L61
DeForest, C. E. 2007, ApJ, 661, 532
DeForest, C. E., Plunkett, S. P., & Andrews, M. D. 2001, ApJ, 546, 569
DeForest, C. E., et al. 1997, Sol. Phys., 175, 393
Del Zanna, G., Rozum, I., & Badnell, N. R. 2008, A&A, 487, 1203
Feng, L., Wiegelmann, T., Inhester, B., Solanki, S., Gan, W. Q., & Ruan, P. 2007a, Sol. Phys., 241, 235
Feng, L., et al. 2007b, ApJ, 671, L205
Fisher, R., & Guhathakurta, M. 1995, ApJ, 447, L139
Fowler, C. M. The Solid Earth: An Introduction to Global Geophysics (2nd ed.; Cambridge Cambridge Univ. Press)
Gabriel, A. H., Abbo, L., Bely-Dubau, F., Llebaria, A., & Antonucci, E. 2005, ApJ, 635, L185
Gabriel, A. H., Bely-Dubau, F., & Lemaire, P. 2003, ApJ, 589, 623
Habbal, S. R. 1992, Ann. Geophys., 10, 34
Howard, R. A., et al. 2008, Space Sci. Rev., 136, 67
Inhester, B. 2006, arXiv:astro-ph/0612649
McComas, D. J., et al. 2000, J. Geophys. Res., 105, 10419
Munro, R. H., & Jackson, B. V. 1977, ApJ, 213, 874
Neukirch, T. 1995, A&A, 301, 628
Newkirk, G. J., & Harvey, J. 1968, Sol. Phys., 3, 321
Patsourakos, S., Pariat, E., Vourlidas, A., Antiochos, S. K., & Wuelser, J. P. 2008, ApJ, 680, L73
Raouafi, N.-E., Harvey, J. W., & Solanki, S. K. 2007, ApJ, 658, 643
Raouafi, N.-E., Petrie, G. J. D., Norton, A. A., Henney, C. J., & Solanki, S. K. 2008, ApJ, 682, L137
Ruan, P., Wiegelmann, T., Inhester, B., Neukirch, T., Solanki, S. K., & Feng, L. 2008, A&A, 481, 827

Saito, K. 1965, PASJ, 17, 1
Thompson, W. T. 2006, A&A, 449, 791
Tu, C.-Y., & Marsch, E. 1997, Sol. Phys., 171, 363
Wang, Y.-M. 1994, ApJ, 435, L153
Wang, Y. M. 1998, ApJ, 501, L145
Wang, Y.-M., & Sheeley, N. R., Jr. 1995, ApJ, 452, 457
Wiegelmann, T., & Inhester, B. 2006, Sol. Phys., 236, 25
Wilhelm, K. 2006, A&A, 455, 697
Wilhelm, K., Dammasch, I. E., Marsch, E., & Hassler, D. M. 2000, A&A, 353, 749
Wilhelm, K., Dwivedi, B. N., & Curdt, W. 2009, arXiv:0902.4167
Wilhelm, K., Marsch, E., Dwivedi, B. N., Hassler, D. M., Lemaire, P., Gabriel, A. H., & Huber, M. C. E. 1998, ApJ, 500, 1023
Wuelser, J.-P., et al. 2004, in Proc. SPIE 5171, Telescopes and Instrumentation for Solar Astrophysics, ed. S. Fineschi & M. A. Gummin (Bellingham, WA: SPIE), 111